1   **Iron "Ore" Nothing: Benthic iron fluxes from the oxygen-deficient Santa Barbara Basin**

2   **enhance phytoplankton productivity in surface waters**

4   **De'Marcus Robinson[1]*, Anh L.D. Pham[1], David J. Yousavich[2], Felix Janssen[3], Frank**

5   **Wenzhöfer[3], Eleanor C. Arrington[4], Kelsey M. Gosselin[5], Marco Sandoval-Belmar[1],**

6   **Matthew Mar[1], David L. Valentine[4], Daniele Bianchi[1], Tina Treude[1,2]***

8   [1]Department of Atmospheric and Oceanic Sciences, University of California Los Angeles, Los

9   Angeles, CA, USA

10   [2]Department of Earth, Planetary, and Space Sciences, University of California Los Angeles, Los

11   Angeles, CA, USA

12   [3]HGF-MPG Joint Research Group for Deep-Sea Ecology and Technology, Alfred Wegener

13   Institute, Helmholtz Centre for Polar and Marine Research, Bremerhaven, Germany

14   [4]Department of Earth Science and Marine Science Institute, University of California, Santa

15   Barbara, CA 93106, USA

16   [5]Interepartment Graduate Program in Marine Science, University of California, Santa Barbara, CA

17   93106, USA

19   *Correspondence: De'Marcus Robinson, demarcus1.robinson@atmos.ucla.edu; Tina Treude,

20   ttreude@g.ucla.edu

23 **Abstract**
24
25 The trace metal iron (Fe) is an essential micronutrient that controls phytoplankton productivity,

26 which subsequently affects organic matter cycling with feedback on the cycling of macronutrients.

27 Along the continental margin of the U.S. West Coast, high benthic Fe release has been

28 documented, in particular from deep anoxic basins in the Southern California Borderland.

29 However, the influence of this Fe release on surface primary production remains poorly

30 understood. In the present study from the Santa Barbara Basin, in-situ benthic Fe fluxes were

31 determined along a transect from shallow to deep sites in the basin. Fluxes ranged between 0.23

32 and 4.9 mmol m^{-2} d^{-1}, representing some of the highest benthic Fe fluxes reported to date. To

33 investigate the influence of benthic Fe release from the oxygen-deficient deep basin on surface

34 phytoplankton production, we combined benthic flux measurements with numerical simulations

35 using the Regional Ocean Model System coupled to the Biogeochemical Elemental Cycling model

36 (ROMS-BEC). For this purpose, we updated the model Fe flux parameterization to include the

37 new benthic flux measurements from the Santa Barbara Basin. Our simulations suggest that

38 benthic Fe fluxes enhance surface primary production, supporting a positive feedback on benthic

39 Fe release by decreasing oxygen in bottom waters. However, a reduction of phytoplankton Fe

40 limitation by enhanced benthic fluxes near the coast may be partially compensated by increased

41 nitrogen limitation further offshore, limiting the efficacy of this positive feedback.

42

1. Introduction

The California Current System (CCS), located off the coasts of Washington, Oregon, and California, is a typical Eastern Boundary Upwelling System, where seasonal upwelling supports a highly diverse and productive marine ecosystem (Chavez and Messié, 2009; Carr and Kearns, 2003). The CCS can be split into three main parts: the main equatorward California Current offshore, a subsurface poleward undercurrent fringing the continental shelf, and a recirculation pattern known as the Southern California Eddy in the Southern California Bight.

In the CCS, both upwelling and large-scale circulation provide essential nutrients to the euphotic zone, where they fuel high rates of net primary production (NPP). While seasonal upwelling dominates north of Point Conception, advection by the CCS provides a major route for nutrient supply to the Santa Barbara Channel in the Southern California Bight (Bray et al., 1999). Following phytoplankton blooms, sinking and degradation of organic matter lead to oxygen consumption and widespread oxygen loss in subsurface waters (Brander et al., 2017; Chavez and Messié, 2009). Along the southern California coast, this oxygen depletion is exacerbated by regional circulation patterns that include transport of low-oxygen waters of tropical origin along the poleward undercurrent (Evans et al., 2020; Pozo Buil and Di Lorenzo, 2017). Oxygan decline is particularly apparent in deep, isolated basins such as those found in the Southern California continental borderland, where the presence of shallow sills limits ventilation of deep waters, and anoxic conditions are often encountered near the bottom (Reimers et al., 1990; Goericke et al., 2015; White et al., 2019).

In the CCS, the trace metal iron (Fe) has been identified as a limiting factor for the growth of phytoplankton (Hogle et al., 2018). Fe is an essential micronutrient that has also a considerable influence on the dynamics of phosphorus and nitrogen in the euphotic zone (Tagliabue et al., 2017). Similar to other nutrients, Fe is transported to the surface by upwelling and circulation. However, Fe supply is generally low in oxygenated environments relative to other macronutrients, reflecting rapid scavenging of insoluble iron-oxide minerals by sinking particles that eventually accumulate in the sediment (Bruland et al., 2001, 2014; Firme et al., 2003; Till et al., 2019). While early studies suggested that Fe inputs to the CCS are dominated by rivers and aeolian deposition (Biller and Bruland, 2013; Johnson et al., 2003), more recent work highlights a combination of sources,

72   including benthic fluxes (Severmann et al., 2010; Noffke et al., 2012; Tagliabue et al., 2017;

73   Wallmann et al., 2022) and ocean currents, which help redistributing Fe in coastal waters (Bray et

74   al., 1999; Boiteau et al., 2019; García-Reyes and Largier, 2010).

75   Benthic release of Fe(II), the reduced and soluble form of Fe, has been recognized as a potential

76   source of Fe to the surface ocean along the continental shelf and slope of the CCS, including the

77   deep basins of the California borderland (John et al., 2012; Severmann et al., 2010). Under hypoxic

78   or anoxic bottom waters, Fe(II) produced in the sediment during microbial organic matter

79   degradation coupled to Fe (III) reduction diffuses across the sediment-water interface and

80   accumulates in the water column (Furrer and Wehrli, 1993; Dale et al., 2015; Severmann et al.,

81   2010; Wallmann et al., 2022). In the CCS, this benthic Fe flux is likely to exceed atmospheric

82   deposition (Deutsch et al., 2021), and may ultimately make its way to the surface by upwelling

83   and vertical mixing, supporting high rates of photosynthesis.

84   The interaction between low bottom water oxygen, Fe(II) release, and transport by the ocean

85   circulation is particularly important in the Santa Barbara Basin (SBB), an oxygen-deficient basin

86   located between the Channel Islands and mainland California in the Southern California Bight.

87   The SBB frequently experiences seasonal anoxia in the bottom water in fall, with irregular oxygen

88   flushing of dense, hypoxic water below the western sill depth (470 m) during winter and spring

89   (Goericke et al., 2015; Sholkovitz and Soutar, 1975; White et al., 2019; Qin et al., 2022). This

90   seasonal flushing reflects either changes in upwelling strength and frequency, or changes in

91   stratification at the sill depth, although the exact cause of the flushing is still unclear (Goericke et

92   al., 2015; Sholkovitz and Gieskes, 1971; White et al., 2019). Lack of oxygen in the deeper parts

93   of the basin supports anaerobic microbial processes in the bottom water and sediment (White et

94   al., 2019), including benthic Fe reduction (Goericke et al., 2015), causing the release of Fe(II) into

95   the water column (Severmann et al., 2010). Ventilation events that re-oxygenate the deep basin, as

96   well as mixing by the vigorous submesoscale circulation (Kessouri et al., 2020), could allow

97   upwelling of this Fe above the sill depth and ultimately to the surface, providing a linkage between

98   benthic processes and upper water-column biogeochemistry. Increased surface primary production

99   supported by this Fe source would in turn drive higher remineralization and oxygen loss in deep

100 waters, thus providing a positive feedback to benthic Fe release. However, with a dearth of benthic

101 Fe flux measurements in the SBB, gaps remain in our understanding of the dynamics and impact

102   of benthic Fe flux in the Southern California Borderland, particularly with respect to its magnitude,
103   dependence on bottom water oxygen, and ability to reach the euphotic zone and influence primary
104   production.

105   In this study, we explore the connection between benthic Fe flux and surface primary production
106   in the CCS, by investigating the influence of enhanced benthic Fe fluxes from low-oxygen waters
107   with a combination of field observations and experiments with a numerical model. We focus on
108   the SBB, where we provide a new set of benthic Fe flux estimates determined by in-situ benthic
109   flux chamber measurements. We combine these new observations with existing data (Severmann
110   et al., 2010) to revise the representation of benthic Fe fluxes in UCLA's Regional Ocean Modeling
111   System coupled to the Biogeochemical Elemental Cycling (ROMS-BEC) model (Deutsch et al.,
112   2021). We then use the model to evaluate the effect of benthic Fe fluxes on surface nutrient
113   consumption and NPP, and compare their impact to that of aeolian Fe deposition in the SBB and
114   beyond.

2. Materials and Methods

2.1 Study Site

Fieldwork in the SBB was conducted between Oct 29 and Nov 11, 2019, during the R/V Atlantis cruise AT42-19. Sampling occurred during the anoxic, non-upwelling season along one bimodal transect with six stations total at depths between 447 and 585 m (**Fig. 1, Table 1**).
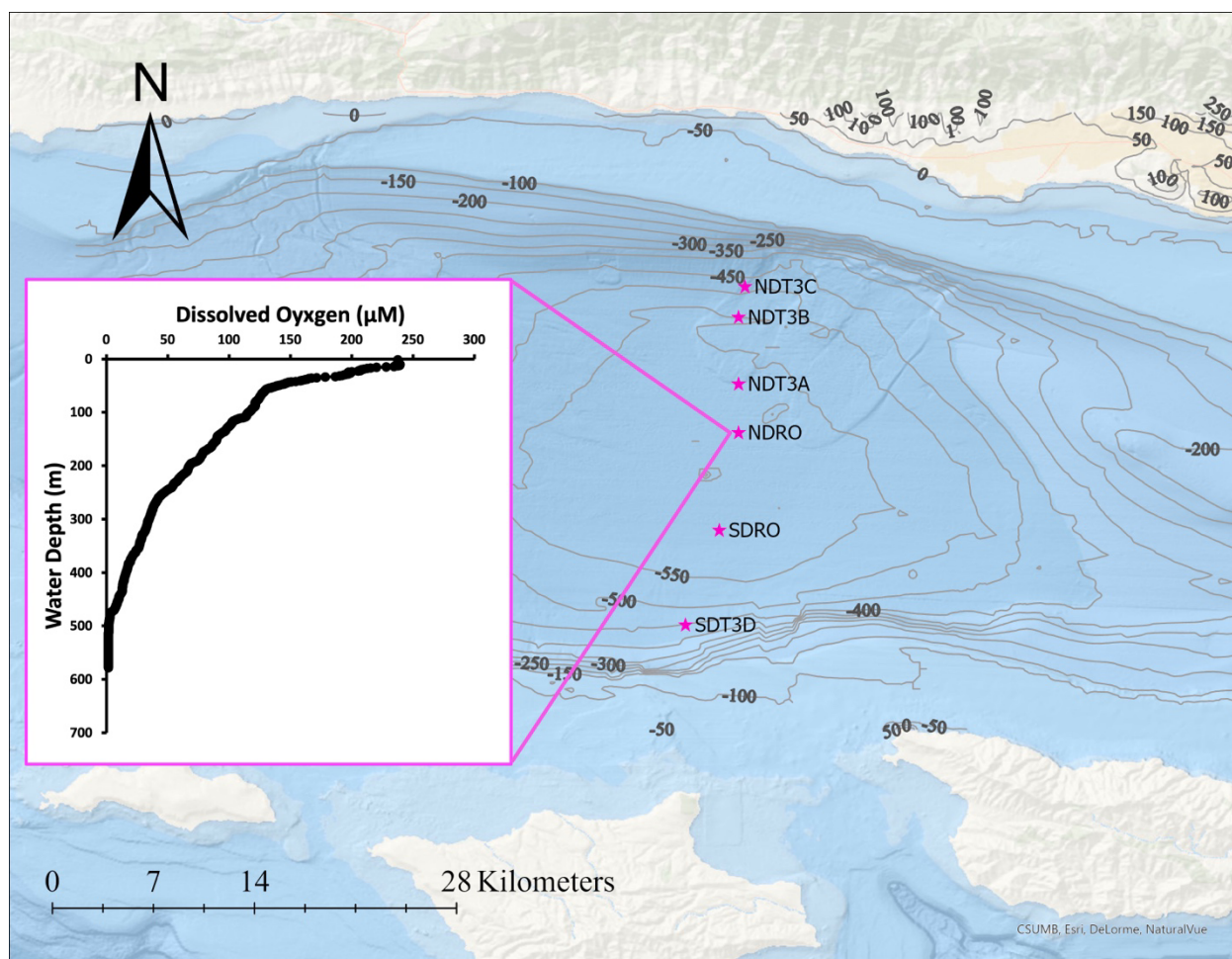
Figure 1. Station locations in the SBB during the AT42-19 expedition with R/V Atlantis. NDT3 (with stations A, B, C) = Northern Depocenter Transect Three, NDRO = Northern Depocenter Radial Origin, SDRO = Southern Depocenter Radial Origin, SDT3 (with station D) = Southern Depocenter Transect Three. The small insert figure displays dissolved oxygen concentrations in the water column at the NDRO station profiled by an optical oxygen sensor attached to the AUV

127   Sentry. The profile was measured at the following position: Latitude 34.2618 N, Longitude -

128   120.0309 E. The map was created using ArcGIS Ocean Basemap, with bathymetric contour lines

129   representing depth information taken from the General Bathymetric Chart of the Ocean (GEBCO)

130   database.

131   Transects were divided into northern (NDT3 = Northern Depocenter Transect Three) and southern

132   (SDT3 = Southern Depocenter Transect Three) sites based on basin geography (**Fig. 1**). Stations

133   were labeled alphabetically from A (deepest) to D (shallowest) according to their location along

134   the transect, except for the deepest stations at the bottom of the basin, which were labeled Northern

135   Depocenter Radial Origin (NDRO) and Southern Depocenter Radial Origin (SDRO).

136   **2.2 Benthic Flux Chambers**

137   Custom-built cylindrical benthic flux chamber systems (Treude et al., 2009) were deployed by the

138   ROV Jason at the six stations (**Fig. 1**). Polycarbonate chambers (19 cm inner diameter) were

139   installed in a small lightweight frame made from fiber-reinforced plastics. A stirrer (Type K/MT

140   111, K.U.M. Umwelt- und Meerestechnik, Kiel, Germany) was used to keep the water overlying

141   the sediment enclosed by the chamber well mixed. One or two replicate chamber systems were

142   deployed at each site. Since sediment in the SBB is quite soft and poorly consolidated, especially

143   towards the deeper stations, frames were fitted with platforms attached to the feet of the frame and

144   with buoyant syntactic foam to reduce sinking into the sediment. A syringe sampler was equipped

145   with 6 glass sampling syringes that were connected with 50 cm long plastic tubes (2.5mm inner

146   diameter, Vygon, Aachen, Germany). Each sampling syringe withdrew 50 mL of the overlying

147   seawater at pre-programmed times. A seventh syringe was used to inject 50 mL of de-ionized

148   water shortly after chambers were deployed to calculate chamber volume from the salinity-drop

149   recorded with a conductivity sensor (type 5860, Aanderaa Data Instruments, Bergen, NO) in the

150   overlying water, following the approach described in (Kononets et al., 2021). Water samples were

151   analyzed for Fe(II) on the ship using a Shimadzu UV-Spectrophotometer (UV-1800), equipped

152   with a sipper unit, following the procedure of (Grasshoff and Ehrhardt, 1999). Fe fluxes were

153   calculated from the slope of linear fits of Fe concentration time series vs. time (**Fig. S1**), multiplied

154   by the chamber volume, and divided by the surface area of the sediment (Kononets et al., 2021).

155   **2.3 Numerical model (ROMS-BEC)**

To explore the impacts of benthic Fe fluxes on surface primary production, we used a well-established ocean biogeochemical model of the CCS (Renault et al., 2016; Deutsch et al., 2021). The physical model component consists of the Regional Ocean Modeling System (ROMS), (Shchepetkin, 2015; Shchepetkin and McWilliams, 2005) a primitive-equation, hydrostatic, topography-following ocean model. As in prior work, the model domain spans the entire U.S. West Coast, from Baja California to Vancouver Island, with a horizontal resolution of 4 km, enough to resolve the mesoscale circulation (Capet et al., 2008). The baseline model configuration was run over the period 1995–2017 with interannually varying atmospheric forcings. We refer the reader to earlier publications (Renault et al., 2021; Deutsch et al., 2021) for a complete description of the model configuration, setup, forcings and boundary conditions used in this study.

ROMS is coupled online to the Biogeochemical Elemental Cycling (BEC) model (Moore et al., 2004), adapted for the U.S. West Coast by (Deutsch et al., 2021). BEC solves the equations for the evolution of six nutrients (nitrate (NO_3^-), ammonium (NH_4^+), nitrite (NO_2^-), silicate (SiO_2), phosphate (PO_4^{3-}), and iron (Fe)), three phytoplankton groups (small phytoplankton, diatoms, and diazotrophs), a single zooplankton group, inorganic carbon, oxygen (O_2), and dissolved organic matter (carbon, nitrogen, phosphorus, and iron). Nutrient and carbon cycles are coupled by a fixed stoichiometry, except for silica and Fe, which use variable stoichiometries (Deutsch et al., 2021; Moore et al., 2001, 2004). The Fe cycle in BEC includes four separate pools: dissolved inorganic Fe (dFe), dissolved and particulate organic Fe, and Fe associated with mineral dust. Of these, only dissolved organic and inorganic Fe are explicitly tracked as state variables, while particulate Fe is treated implicitly by resolving vertical sinking particle fluxes (Moore et al., 2001; Moore and Braucher, 2008). Four main processes control the cycle of Fe in the model: atmospheric deposition, biological uptake and remineralization, scavenging by sinking particles, and release by sediment. The atmospheric dFe deposition is based on the dust climatology of (Mahowald et al., 2006), and dissolution rates from (Moore and Braucher, 2008). Different from (Deutsch et al., 2021), we re-evaluated the dependence of benthic dFe fluxes on bottom water O_2 concentrations in the California margin based on a merged dataset that combines our measurements from the SCB, with those presented in (Severmann et al., 2010) (see Section 2.5). The model Fe scavenging scheme removes dFe from the water column at a rate proportional to sinking particle fluxes and dFe concentrations, assuming a uniform concentration of 0.6 nM of Fe-binding ligands (Moore et al., 2004; Moore and Braucher, 2008). Accordingly, scavenging rates increase strongly at dFe

187   concentrations greater than 0.6 nM, and vice versa rates decrease strongly below 0.5 nM (**Fig. S2**).

188   Note that, while simplistic, this formulation is still widely adopted by global ocean

189   biogeochemistry models (Tagliabue et al., 2014, 2016), although improvements have been

190   proposed (Moore and Braucher, 2008; Aumont et al., 2015; Pham and Ito, 2019, 2018).

191   As shown in previous work, the model captures the main patterns of physical and biogeochemical

192   variability in the CCS, providing a representation of nutrient cycles and NPP in good agreement

193   with observations (Renault et al., 2021; Deutsch et al., 2021). We further evaluate the model

194   against an extended set of dissolved Fe measurements for the CCS (see Sections **2.4** and **3.1**).

195   **2.4 Fe dataset along the U.S. West Coast**

196   To assess the ability of the model to capture observed patterns in dFe along the U.S. West Coast,

197   we gathered available dFe concentration measurements from published studies, including a global

198   compilation (Tagliabue et al., 2016), regional programs such as CalCOFI, CCE-LTER, IRNBRU

199   and MBARI cruises (Bundy et al., 2016; Hogle et al., 2018; Johnson et al., 2003; King and

200   Barbeau, 2011), and other individual studies (Biller and Bruland, 2013; Boiteau et al., 2019; Bundy

201   et al., 2014, 2015, 2016; Chappell et al., 2019; Chase, 2002; Chase et al., 2005; Firme et al., 2003;

202   Hawco et al., 2021; John et al., 2012; Till et al., 2019). In the final compilation, we define dFe as

203   the sum of the dissolved Fe and dissolvable Fe, based on the definitions used in each publication.

204   Different studies used different filter sizes to define the dFe pool, most commonly 0.20, 0.40, and

205   0.45 µm, and different sampling methods, such as bottles, pump systems and/or surface tows. In

206   some studies, samples were briefly acidified before being analyzed. Despite the differences in

207   sampling and measurement approaches, we found that these datasets generally agreed with each

208   other, suggesting that the final compilation accurately represents the dFe distribution along the

209   U.S. West Coast. The final dataset includes observations from 1980 to 2021, with most samples

210   collected between 1997 and 2015, and from the upper 100 m of the water column.

211   **2.5 Experimental Design**

212   To evaluate the impact of Fe fluxes from low-O_2 sediment in the SBB on surface biogeochemistry,

213   we designed a suite of model sensitivity experiments with ROMS-BEC in which external sources

214   of Fe are modified relative to a baseline simulation. Accordingly, we run the following model
215   experiments:

216   ***High-flux****:* This experiment is the baseline model simulation, using a Fe flux parameterization
217   calculated as an exponential fit to a data set of benthic Fe fluxes consisting of the new benthic
218   measurements from AT42-19 and previous observations from the U.S. West Coast (Severmann et
219   al., 2010) (see Section 3.2), thus updating the parameterization by (Deutsch et al., 2021). Benthic
220   Fe release follows the equation:

221    $\log_{10}(\text{Fe}) = 2.86 - 0.01 \cdot O_2$ (Equation 1)

222   Where O_2 is the concentration of oxygen in mmol m^{-3} and (Fe) is the Fe flux in μmol m^{-2} d^{-1}. This
223   revised formulation is only applied in the SBB where we performed our measurements, while a
224   different formulation, solely based on data by (Severmann et al., 2010) is used outside of the SBB:

225    $\log_{10}(\text{Fe}) = 2.6178 - 0.0128\, O_2$ (Equation 2)

226   For this parameterization, we corrected a model bias that resulted in modeled bottom O_2
227   concentrations greater than 30 mmol m^{-3} over most of the deep basins where observations indicated
228   lower concentrations, down to oxygen-free conditions (**Fig. S3**). We therefore reduced modeled
229   bottom water O_2 concentrations in the Southern California Borderland by 30 mmol m^{-3}, based on
230   the average difference between model and observed O_2 in the region. This correction is crucial to
231   producing realistic benthic Fe fluxes under the anoxic conditions observed in the SBB, rather than
232   fluxes at O_2 concentrations of 30 mmol m^{-3}.

233   ***Hypoxia-off:*** The purpose of this experiment is to evaluate the importance of enhanced Fe fluxes
234   under low-O_2 conditions in the SBB. Benthic Fe fluxes are calculated as in *High-flux* experiment
235   (Equation 2), but they are capped at a constant value when O_2 decreased below a threshold of 65
236   mmol m^{-3}, which we chose as representative of hypoxic conditions (Deutsch et al., 2011). This
237   change is applied only to in the SBB, and effectively bounds the benthic Fe release at 1.48 μmol
238   m^{-2} d^{-1} when O_2 drops below the threshold for hypoxia.

239   ***Dust-off***: The purpose of this experiment is to evaluate the importance of aeolian Fe deposition in

240   the CCS, and to compare it with the benthic Fe fluxes. In this experiment, the atmospheric Fe

241   deposition is set to zero; all other settings are identical to the *High-flux* experiment.

242   The baseline (*High-flux*) model simulation is run from 1995 to 2017. The other two model

243   sensitivity experiments (*Hypoxia-off* and *Dust-off)* are branched off from the *High-flux* simulation

244   in year 2008 and run separately for 10 additional years (2008-2017). All model experiments use

245   the same set of forcings and initial conditions. Results from the final 3 years (2015-2017) of the

246   *Hypoxia-off* and *Dust-off* simulations are averaged and analyzed by comparing differences in

247   biogeochemical fields (Fe, NO_3^-, and NPP) to the final 3 years of the *High-flux* run.

3. Results

3.1 In-situ benthic Fe fluxes and model parameterization

Benthic Fe fluxes from in-situ benthic chamber measurements during the AT42-19 expedition are shown in **Table 1**. High Fe flux was recorded at the anoxic depocenter stations (4.90 and 3.92 mmol m^{-2} d^{-1} at SDRO and 3.49 mmol m^{-2} d^{-1} at NDRO). Fe fluxes at the shallower hypoxic stations (NDT3C, NDT3B, and SDT3D) were an order of magnitude lower. The Fe flux at the hypoxic NDT3A station between NDRO and NDT3B was approximately half the flux observed at the depocenter.

Table 1. Station details and geochemical parameters determined during the AT42-19 expedition. Benthic Fe fluxes were determined using in-situ benthic chambers. Dissolved O$_2$ concentrations were measured in the water column at 10 m above the seafloor using a Seabird optode sensor attached to the ROV Jason. At stations with two benthic chamber deployments (NDT3A and SDRO), O$_2$, geographical coordinates, and depth were averaged as there were only minimal differences between the two chamber deployments.

Station	Fe Flux [mmol m^{-2} d^{-1}]	O$_2$ [mmol m^{-3}]	Latitude [N]	Longitude [E]	Depth [m]
NDT3C	0.23 (n=1)	5.3	34.3526	-120.0160	499
NDT3B	0.36 (n=1)	6.8	34.3336	-120.0188	535
NDT3A	1.73; 1.20 (n=2)	9.6	34.2921	-120.0258	572
NDRO	3.49 (n=1)	0.0	34.2618	-120.0309	581
SDRO	4.90; 3.92 (n=2)	0.0	34.2011	-120.0446	586
SDT3D	0.58 (n=1)	9.6	34.1422	-120.0515	446

Trends in the Fe fluxes suggest modulation by O$_2$ concentration, water depth, and/or bathymetry. We also note that observed oxygen concentration represents a snapshot of bottom water conditions, while Fe fluxes likely reflect the oxygenation history at any given site. We observed a decrease in the Fe flux with a decrease in water depth (**Fig. 2**). There was also a slight trend of higher Fe fluxes with lower O$_2$ concentrations (most pronounced when O$_2$ reaches zero); however, since O$_2$

268   concentrations were relatively low at all stations (<10 mmol m^{-3}) it is difficult to distill a clear

269   pattern based on the small dataset. Notably, the NDT3A station showed a high Fe flux despite

270   exhibiting the same O_2 concentration as the shallower station SDT3D. Basin bathymetry may also

271   contribute to observed differences in the flux. For instance, the deeper depocenter and A-station

272   showed higher averaged fluxes than the B, C, and D stations. We further noticed differences

273   between the north and south extension of the transect. The southern stations (SDRO and SDT3D)

274   showed a higher Fe flux than the northern stations (NDRO and NDT3C).
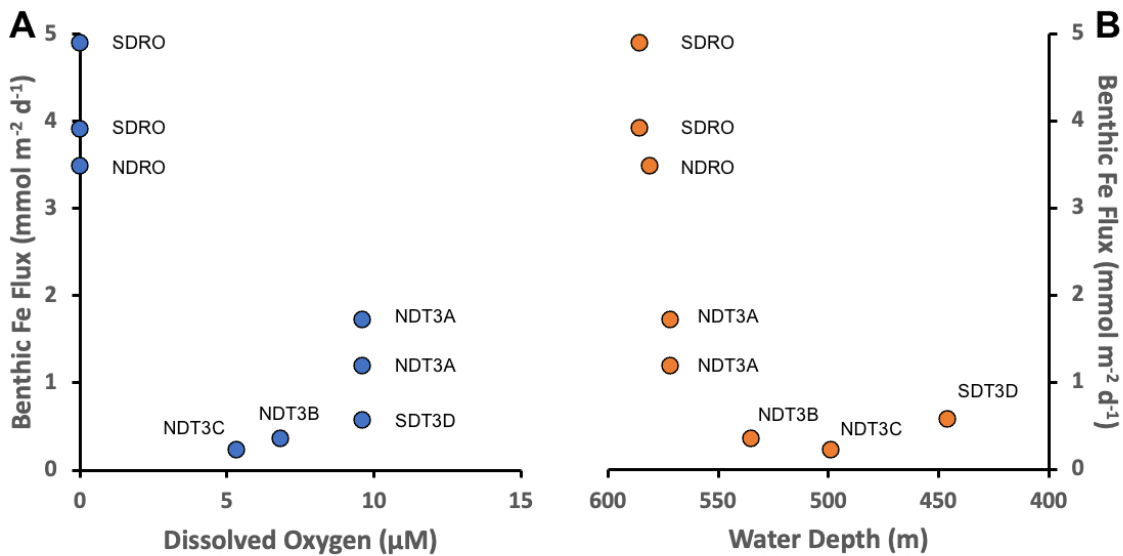
275

276   **Figure 2**. Benthic in-situ Fe fluxes. A: Fluxes as a function of O_2. B: Fluxes as a function of

277   (station) water depth. Note that water depth is shown from deep to shallow depths. See Table 1 for

278   station details.

279   We combined Fe fluxes determined during AT42-19 with previous estimates along the CCS, as

280   compiled by (Severmann et al., 2010), and analyzed them as a function of bottom water O_2 (**Fig.**

281   **3**). Pooled together, the measurements can be described reasonably well by an exponential increase

282   of Fe fluxes with declining bottom water O_2 (Severmann et al., 2010), although significant

283   variability around an exponential fit remains. This relationship is consistent with the Fe flux

284   parameterization adopted in the ROMS-BEC model (Deutsch et al., 2021). Several observations

285   from the AT42-19 cruise (red dots in **Fig. 3**) exceed the range of previous measurements (blue

286   dots in **Fig. 3**), likely owing to the anoxic or near-anoxic conditions in the water. Relative to the

287   exponential fit to the dataset by (Severmann et al., 2010) (yellow line in **Fig. 3**, see Equation 2)

288   the revised fit to the pooled data (purple line in **Fig. 3**, see Equation 1) expands Fe fluxes by

289   approximately a factor of two at O_2 concentrations close to zero, but decreases the magnitude of

290   the Fe fluxes at concentrations above approximately 130 mmol m^{-3}.

291   **3.2 Model evaluation: High flux simulation**

292   The *High-flux* simulation captures the magnitude and patterns of the observed dFe distribution in

293   the upper ocean (**Fig. 4**), consistently with our knowledge of the ocean Fe cycle. In both model

294   and observations, dFe concentrations are low at the surface, as a result of phytoplankton uptake,

295   and increase gradually in subsurface waters due to organic matter remineralization in the water

296   column and at the seafloor, and benthic Fe fluxes from the sediment **(Fig. S4)**. The highest dFe

297   concentrations are found along the coast, likely related to high surface productivity and shallow

298   carbon export and remineralization, combined with basin bathymetry and O_2 deficiency. In the

299   open ocean, dFe concentrations are low in both model and observations, reflecting a combination

300   of phytoplankton uptake, scavenging by sinking particles, and low external inputs.
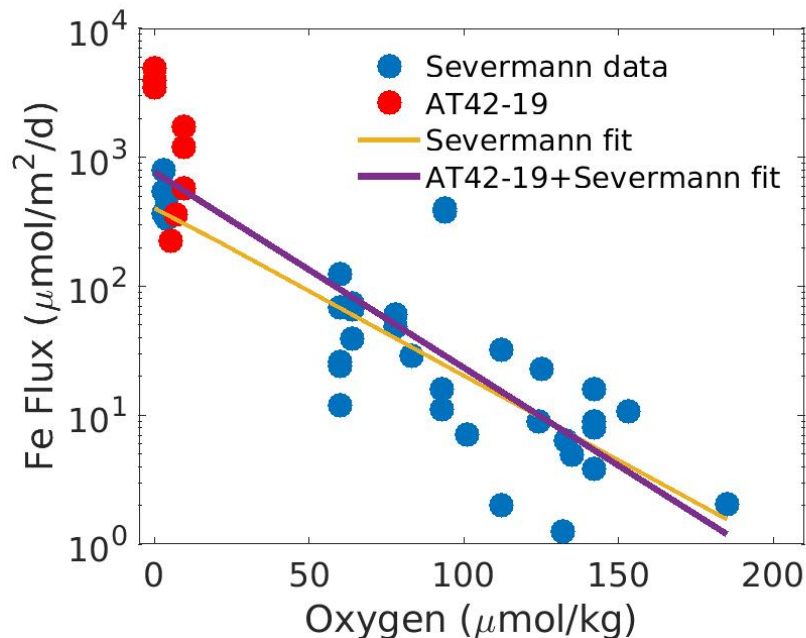
301

302   **Figure 3**. Combined benthic Fe flux data as a function of bottom oxygen. Blue dots show data

303   from the compilation by (Severmann et al., 2010); red dots measurements from the AT42-19

304   cruise. The yellow line shows an exponential fits to the dataset by (Severmann et al., 2010)

305 (Equation 2). The purple line shows an exponential fit to the combined dataset (Equation 1). Note
306 the logarithmic scale used for the y-axis.
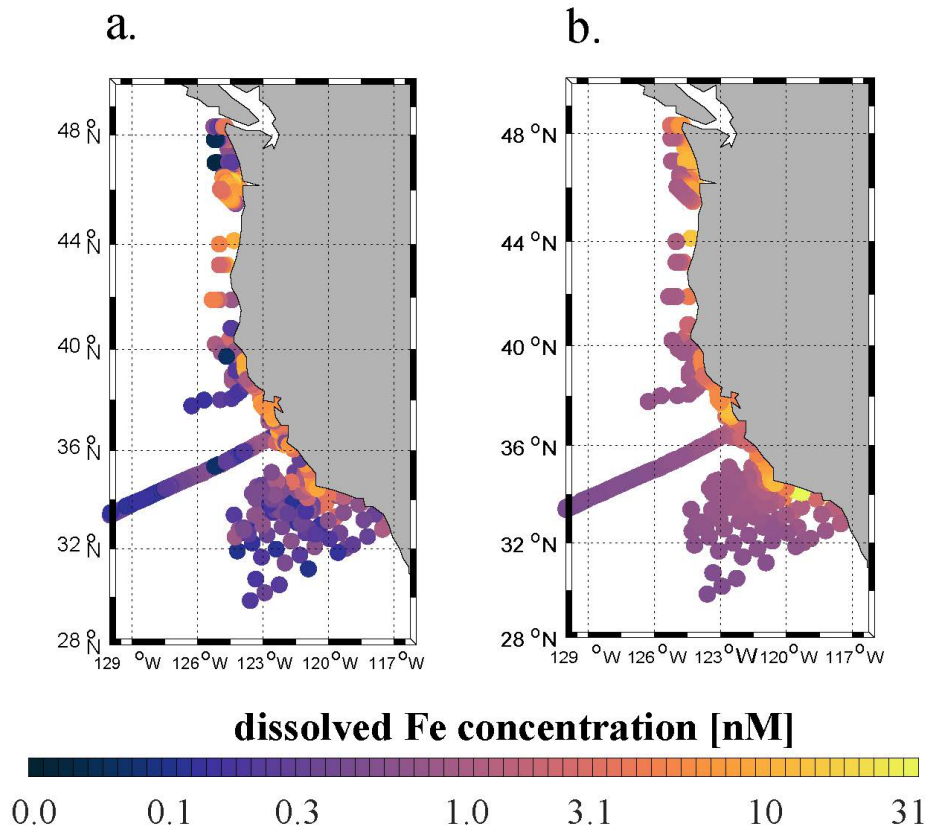
307

308

309 **Figure 4**. (a) Observed dFe concentrations (nM) from the U.S. West Coast compilation (see
310 Section **2.4**) averaged between 0 and 100 m depth. (b) Annual mean modeled dFe concentrations
311 (nM) averaged between 0 and 100 m depth, sampled at the same locations as the observations in
312 panel (a).

313 Observational limitations prevent a more detailed validation of subsurface dFe patterns.
314 Measurements of dFe concentrations in subsurface and deep waters (> 100 m) are currently very
315 sparse in the CCS region and Southern California Borderland. Most of the dFe measurements for
316 the SBB come from limited sampling conducted quarterly as part of selected CalCOFI (California
317 Cooperative Oceanic Fisheries Investigations) cruises (King and Barbeau, 2011). These samples
318 mostly focus on the mixed layer and are too sparse in space and time to capture the effects of deep-

319 water renewal events that ventilate the anoxic basins and allow uplifting and transport of deep
320 waters towards the surface.

321 The agreement of the model dFe with observations (correlation coefficient R=0.22, p<0.01) is
322 similar to that of other ocean biogeochemical models (Tagliabue et al., 2016). The model tends to
323 underestimate the sharp dFe gradient between coastal and open ocean waters, overestimating dFe
324 in the open ocean and producing too uniform concentrations offshore and at depth (**Fig. 4**). These
325 biases are likely related to the simple Fe scavenging scheme, which assumes a constant Fe-binding
326 ligand concentration of 0.6 nM. The small number and episodic nature of in-situ measurements
327 may also explain some of the mismatches between model and observations.

328 At the scale of the CCS, the *High-flux* simulation produces lower surface dFe in the southern part
329 of the domain (33°N to 36°N), and higher surface concentration in the northern part (40°N to
330 45°N) and near the central coast (**Fig. 5a**). While these patterns reflect a combination of internal
331 Fe cycling and external inputs, the elevated dFe in the northern CCS, in particular offshore, can be
332 partly attributed to higher aeolian deposition in that region (**Fig. S5)** as well as coastal inputs from
333 the Juan De Fuca strait (Deutsch et al., 2021).

334 The model reproduces the typical signature of coastal upwelling, with higher concentrations of
335 NO_3^- nearshore in the central coast (36°N-40°N) and low concentrations in the Southern California
336 Bight and offshore (**Fig. 5b**). Similarly, the model reproduces high values of NPP near the coast,
337 in particular along the central coast, and rapidly decreasing values offshore (**Fig. 5c**). Relative to
338 previous modeling work (Deutsch et al., 2021) our simulations generate somewhat lower surface
339 NO_3^- concentrations close to the coast, and sharper NPP gradients between the nearshore and
340 offshore regions, which are consistent with the rapid decrease in primary productivity and
341 chlorophyll shown by both satellite-based estimates and *in situ* data (Deutsch et al., 2021). These
342 changes likely reflect the higher benthic Fe fluxes in our simulations (Equation 1), which increase
343 phytoplankton productivity and promote nutrient drawdown near the coast.

344
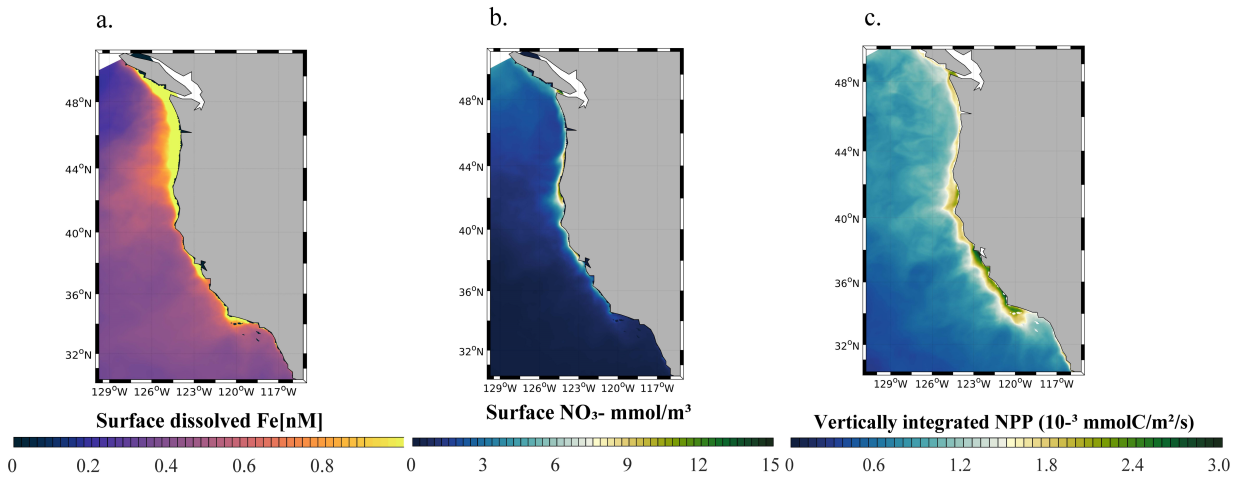
Fig. 5. (a) Surface dFe concentration, (b) surface NO_3^- concentration, and (c) vertically integrated
net primary production (NPP) from the *High-flux* model simulation.

3.3 Hypoxia-off: Impact of benthic Fe flux from low-oxygen bottom water

We quantify the importance of benthic Fe fluxes from low-O_2 bottom waters in the Southern
California Borderland by analyzing results from the *Hypoxia-off* experiment, in which we cap the
high benthic Fe flux at a constant value (1.48 μmol m^{-2} d^{-1}) when O_2 declines below hypoxic
conditions (65 mmol m^{-3}, see Section 2.5) (**Fig 6**).
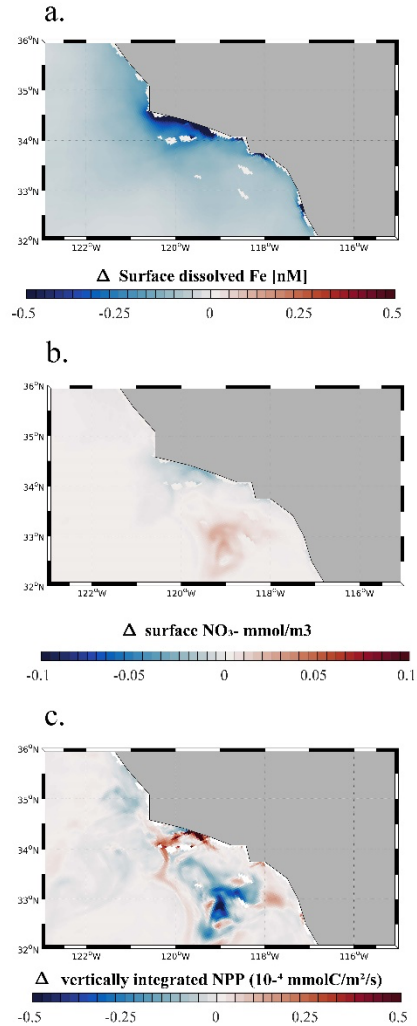
Figure 6. (a) Surface dFe anomalies, (b) Surface NO_3^- anomalies, and (c) vertically integrated net primary production (NPP) from the *Hypoxia-off* model run relative to the *High-flux* model run. The maps focus on the region around the SBB.

As expected, a decrease in benthic Fe flux from the anoxic basins in the *Hypoxia-off* simulation leads to a decrease in the surface dFe concentration (**Fig. 6a**). This decrease is particularly significant along the coast of the SBB, but also extends slightly into the open ocean (**Fig S6**). This trend indicates that dFe released from low-O_2 sediment is effectively transported to the surface and offshore, where it can affect primary production. The decrease in surface dFe caused by reduced benthic release causes a decline in NPP near the coast (**Fig. 6c**), where phytoplankton rely the most on benthic-derived Fe. NPP also shows a patchy increase in some regions,

366   especially between 32°N and 33°N and between 34°N and 35°N. This patchy increase can be

367   explained by the relative importance of Fe vs. N limitation along a cross-shore productivity

368   gradient. While near the SBB coast, phytoplankton is frequently Fe limited (up to 50% of the

369   time in the model), especially following upwelling events, it tends to be almost exclusively N-

370   limited moving offshore (Deutsch et al., 2021). This limitation pattern is consistent with

371   observations from (King and Barbeau, 2011), who show that N:Fe ratios decrease moving from

372   the coast to the open ocean (i.e., N is likely more limiting than Fe offshore). As Fe limitation

373   reduces NPP near the coast in the *Hypoxia-off* experiment, NO_3^- utilization also declines, so that

374   more NO_3^- can accumulate in surface waters (**Fig. 6b**). Shallow transport of excess NO_3^- in

375   mesoscale eddies can further fertilize offshore waters (Damien et al., 2023), releasing local N

376   limitation and fueling an increase in NPP (**Fig. 6c**).

377   **3.4 Dust-off: Role of atmospheric Fe deposition**

378   We evaluate the importance of aeolian Fe sources in the *Dust-off* simulation, in which

379   atmospheric Fe deposition is set to zero. In this experiment, surface dFe decreases everywhere in

380   the CCS, but the decrease is particularly evident in the open ocean and the northern part of the

381   domain (**Fig. 7a**). This dFe decrease leads to a widespread reduction in NPP in the northern CCS

382   (40°N to 48°N, **Fig. 7c**), with stronger negative anomalies away from the coast. The decline in

383   NPP is accompanied by a broad decrease in NO_3^- utilization, particularly evident offshore, where

384   phytoplankton rely mostly on Fe delivery by dust. In contrast, we observe a broad increase in

385   NPP in the southern CCS (south of 40°S) and in coastal areas, likely reflecting increased

386   availability of NO_3^- transported southward by the broad California Current. The response of NPP

387   in coastal areas and the southern CCS, when the dust deposition of Fe is set to zero, demonstrates

388   that phytoplankton in those regions relies mostly on benthic Fe fluxes, rather than dust

389   deposition, as the main source of Fe.

390

391
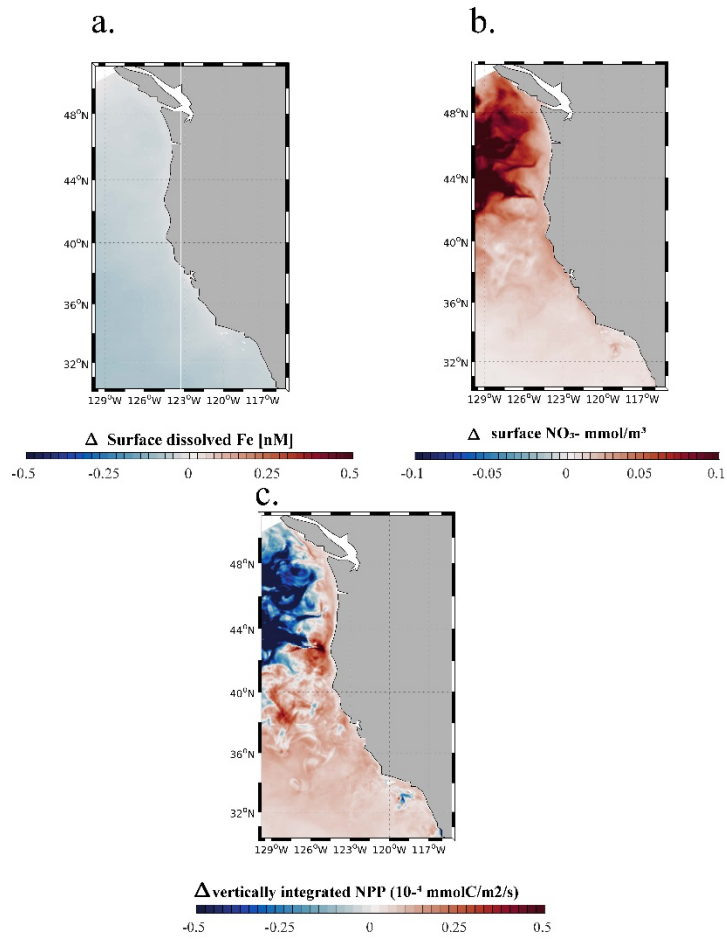
Figure 7. (a) Surface dissolved Fe, (b) surface NO$_3^-$ anomalies, and (c) vertically integrated net primary production (NPP) from the *Dust-off* model run relative to the *High-flux* model run.

4. Discussion

4.1 Benthic Fe flux feedbacks on SBB biogeochemistry

The influence of bottom water O_2 concentration on the exchange of solutes between the sediment and the water column has been well documented (Soetaert et al., 2000; Sommer et al., 2016; Testa et al., 2013). Under hypoxic or anoxic bottom water conditions, organic matter sedimentation sustains anaerobic respiration at the sediment-water interface and in the sediment (Furrer and Wehrli, 1993; Middelburg and Levin, 2009a). Reduced compounds accumulate in pore waters forming chemical gradients (Widdows and Brinsley, 2002) that result in the flux of solutes such as Fe(II) out of the sediment, and their accumulation in bottom water (Jørgensen and Nelson, 2004; McMahon and Chapelle, 1991; Middelburg and Levin, 2009b; Yao et al., 2016). Similar conditions are observed in the SBB, where high sedimentation rates, water column denitrification below the sill depth, and high pore-water concentrations of sulfide and Fe(II) have been observed (Behl and Kennett, 1996; Bray et al., 1999; Goericke et al., 2015; Sholkovitz and Soutar, 1975; Sigman et al., 2003; White et al., 2019).
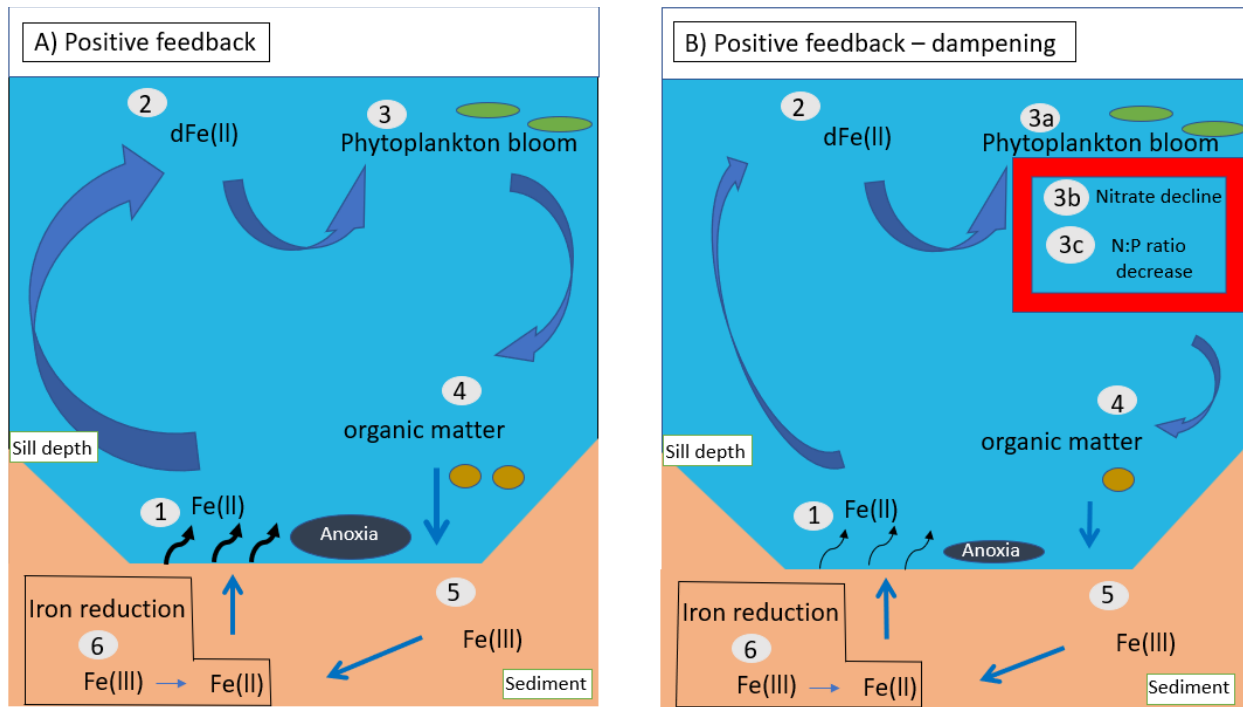
Figure 8. Schematic illustrating feedback loops between benthic Fe release, nutrient cycles, and productivity in the Santa Barbara Basin. (a) Positive feedback loop: 1. Benthic Fe is released into the oxygen-poor bottom water. 2. Upwelled Fe reaches the surface ocean increasing dissolved Fe concentrations. 3. Dissolved Fe is assimilated by phytoplankton, fueling blooms and production of organic matter and siderophores, i.e., ligands used to chelate ferric iron. 4. Organic matter is exported from the surface to the deep ocean. 5. Organic matter accumulates at the sediment-water interface. 6. During remineralization, iron-reducing bacteria reduce Fe(III) to Fe(II), increasing benthic dFe release. (b) Positive feedback loop – dampening: 1-3 (not including 3b and 3c) and 4-6 are identical to (a). Parts 3b and 3c illustrate the decline of NO_3^- at the surface caused by the reduction in Fe limitation, which together with increased denitrification in anoxic waters and sediment would limit the potential increase in primary production and export from the surface caused by Fe fertilization. Together with enhanced release of phosphate from anoxic sediment, a reduction in the available NO_3^- could also reduce the N:P ratio of phytoplankton. Ultimately, the effect of a decrease of NO_3^- on export and remineralization of organic matter would limit the increase of benthic Fe(II) fluxes, dampening the positive feedback.

429 The intense flux of dFe from the sediment suggests the potential for biogeochemical feedbacks in
430 the SBB and more broadly in the CCS (as shown by Figs. 5 – 7). Under a positive feedback scenario
431 (illustrated in Fig. 8a), anoxic and nearly anoxic bottom water conditions facilitate Fe(II) diffusion
432 from the sediment into the bottom water. In the SBB, this Fe eventually reaches the surface via
433 upwelling and mixing processes, which are likely enhanced in the presence of complex bathymetry
434 and islands in the Southern California Bight (Kessouri et al., 2020). This additional dFe input
435 fertilizes coastal waters and increases primary production. Newly formed organic matter
436 eventually sinks towards the seafloor as a rain of organic particles, supporting low-oxygen
437 concentrations in the bottom water, and fueling anaerobic respiration, including Fe reduction, in
438 the sediment. This chain of processes thus represents a positive feedback loop that maintains high
439 Fe(II) release from the sediment, as long as the bottom water remains hypoxic or anoxic (Mills et
440 al., 2004; Noffke et al., 2012; Sañudo-Wilhelmy et al., 2001; Dale et al., 2015; Wallmann et al.,
441 2022).

442 Our simulations also indicate the potential for complex biogeochemical responses between Fe,
443 NO_3^- and NPP, which could limit the effects of these feedbacks. Specifically, the positive feedback
444 loop is damped in our conceptual model by increased NO_3^- limitation and elevated N-loss in anoxic
445 sediments under oxygen-deficient bottom waters at higher Fe supply (illustrated by Fig. 8b), which
446 would in turn limit the increase in NPP. Transport of N-depleted coastal waters can further reduce
447 NPP offshore, counteracting the positive feedback. In addition, the positive feedback would be
448 also damped by Fe scavenging, which is magnified at high dissolved Fe concentrations, unless Fe-
449 binding ligands also increase. This damping effect is particularly strong in our model, where a
450 constant ligand concentration of 0.6 nM is used, above which scavenging rapidly increases
451 (Section 2). Such a negative feedback between scavenging and benthic Fe fluxes is consistent
452 with the global modeling study by Somes et al. (2021).

453 Additional processes may further modulate these feedback loops. Increased anoxia in bottom water
454 and sediment favors the removal of fixed N by denitrification (Goericke et al., 2015; White et al.,
455 2019). Upwelling of NO_3^--depleted waters would then reduce surface productivity by increasing
456 N limitation (Gruber and Deutsch, 2014). Release of Fe(II) from the sediment could also impact
457 phosphate dynamics. Phosphate is scavenged by Fe during oxidation of Fe(II) in the water column
458 and sediment because of the ability of Fe(III) minerals to bind it. After burial, phosphate is released

459 due to reduction of solid Fe(III) minerals to dissolved Fe(II), and diffuses upward to be either re-

460 adsorbed by Fe(III) at the oxic sediment-water interface, or released to the bottom water under

461 anoxic conditions (Dijkstra et al., 2014). The latter scenario is consistent with our in-situ benthic

462 flux chamber measurements revealing increased phosphate release from the sediment with

463 increased depth in the SBB (Yousavich et al., 2023). Higher release of phosphate into the water

464 column, and transport to the surface, could decrease the N:P ratio of phytoplankton, especially

465 downstream of waters where denitrification occurred (Deutsch et al., 2007). In the presence of N

466 limitation, these conditions could favor the activity of nitrogen-fixing microorganisms (Mills et

467 al., 2004; Noffke et al., 2012; Sañudo-Wilhelmy et al., 2001), which could further modulate

468 surface NPP (Deutsch et al., 2007).

469 **4.2 Contribution of physical transport on surface Fe**

470 Our numerical experiments suggest that Fe released into the deep SBB can reach surface waters

471 and fertilize them. This finding highlights the critical role of bottom water upwelling and mixing

472 in the deep basins of the Southern California Borderland. There is ample literature describing

473 seasonal surface circulation and bottom water renewal and their effect on nutrients in the SBB

474 (Bray et al., 1999; Hendershott and Winant, 1996; Sholkovitz and Gieskes, 1971). However, the

475 frequency and rate of seasonal bottom water flushing events, and the processes responsible for

476 vertical mixing and upwelling across hundreds of meters remain poorly understood (Shiller et al.,

477 1985; Sholkovitz and Gieskes, 1971; White et al., 2019). It is likely that interaction between wind-

478 driven upwelling events and submesoscale eddies, which are particularly intense inside the Santa

479 Barbara Channel (Kessouri et al., 2020), favors upward mixing of deep bottom water in the wake

480 of flushing events, connecting deep bottom waters to the surface.

481 **4.3 Quantifying expansion of anoxia in the SBB**

482 Changes in source waters and global O_2 loss have contributed to decreasing O_2 levels throughout

483 the Southern California Bight and the SBB (Zhou et al., 2022). With the outlook of a continuing

484 decline in oceanic O_2 (Bopp et al., 2013; Kwiatkowski et al., 2020), quantifying the expansion of

485 hypoxic and anoxic zones in the SBB is vital to understand the dynamics and fate of Fe(II) and

486 other reduced compounds, such as ammonium and hydrogen sulfide, in deep low-oxygen waters.

487 In the SBB, bottom water renewal events have experienced a decline in frequency and magnitude,

488   driving an expansion of hypoxic and anoxic conditions in deep waters (White et al., 2019). This

489   expansion has led to an increase in anaerobic reactions, such as denitrification in the water column

490   (White et al., 2019) as well as sulfur cycling in the sediment (Valentine et al., 2016). Expansion

491   of low O_2 waters could intensify the positive feedback loop between Fe release, NPP and O_2 loss

492   (**Fig. 8)**. However, to date, despite growing evidence for more frequent anoxia, there is no clear

493   quantitative record of the vertical or horizontal expansions of oxygen-deficient waters in the SBB.

5. Conclusion

Our field campaign in the SBB measured a remarkably high flux of Fe(II) from the sediment (0.23 – 4.9 mmol m^{-2} d^{-1}), greater than in previous studies from this region (Severmann et al., 2010) and from other oxygen minimum zones (Dale et al. 2015; Homoky et al. 2021). While these observations are based on snapshots of O_2 and Fe fluxes, they have implications for the temporal variability of Fe supply. High benthic Fe fluxes are observed during the anoxic fall season, while seasonal flushing in winter and spring likely decreases them by increasing bottom water O_2 and Fe oxidation and retention near the sediment.

Using a series of simulations with an ocean biogeochemical model, we show that this high Fe release from deep, low-oxygen sediment can reach the surface and impact nutrients and productivity in the SBB and the Southern California Bight, where Fe is often limiting (Hogle et al., 2018). We also highlight the impacts of coastal Fe inputs on waters further offshore. While phytoplankton in coastal areas directly benefits from Fe fertilization, increased NO_3^- utilization in coastal waters can increase N-limitation of phytoplankton further downstream in open-ocean areas. Thus, benthic Fe fluxes can modulate Fe and NO_3^- limitation in ways that partially counteract one another along the cross-shore productivity gradient of the CCS. Our simulations also suggest that Fe inputs from atmospheric deposition are mostly important in the open ocean north of 40°N, where phytoplankton rely on Fe delivery by dust. However, we also show that changes in atmospheric Fe deposition can affect ocean productivity in the southern CCS by altering NO_3^- utilization further downstream. Our results support the idea that benthic Fe fluxes are the major source of Fe in the southern CCS and are supplemented by atmospheric deposition in northwestern and offshore waters, leading to relatively high NPP coastwide.

We suggest that benthic Fe fluxes from deep anoxic basins reach the surface in the SBB, contributing to feedbacks between Fe and NO_3^- limitation and NPP. Specifically, high Fe fluxes from low-oxygen sediment support higher NPP near the coast, in turn leading to increased respiration and O_2 loss at depth, maintaining high Fe release. This positive feedback is damped by increased NO_3^- limitation, which reduces NPP downstream of coastal regions. This benthic-pelagic coupling demonstrates the importance of sediment-derived Fe fluxes on the coastal ecosystem of the CCS, and the role of vertical transport processes in connecting deep environments to surface

523 waters along continental margins. Our results are thus consistent with previous work from the

524 Peruvian coastal upwelling (Wallmann et al., 2022), suggesting that oceanic O_2 loss could drive

525 an increase in benthic Fe fluxes, enhancing local productivity and leading to further O_2 loss. This

526 positive feedback could be stabilized by loss of fixed nitrogen under expanded anaerobic

527 conditions.

528 It is likely that feedbacks of the type highlighted by (Wallmann et al., 2022) and our work in the

529 SBB are at play more broadly along low-oxygen upwelling systems and coastal OMZ. Further

530 studies should focus on the coupling between benthic processes and Fe and nutrient cycling in

531 these regions. For example, fixed nitrogen loss by denitrification and enhanced release of

532 phosphorous under low-oxygen bottom water are likely to further modulate these interactions.

533 Seasonal studies based on stable isotope, radiotracer, and geochemical techniques are required to

534 track the fate and transport of nutrients in low-O_2 coastal regions, clarifying the dynamics and

535 sensitivities of the underlying microbial metabolisms. Ocean biogeochemical models for regional

536 and global studies should incorporate new observations of benthic fluxes and their sensitivity to

537 bottom O_2 and other environmental variables. This would expand the ability of models to better

538 capture the effects of long-term oceanic O_2 loss, and the feedbacks between benthic nutrient fluxes

539 and surface productivity.

Acknowledgements

We thank the captain and crew of R/V Atlantis, the crew of ROV Jason, the crew of AUV Sentry, and the science party of research cruise AT42-19 for their technical and logistical support. We thank Q. Qin, M. O'Beirne, A. Mazariegos, X. Moreno, and A. Eastman for assisting with shipboard analyses. Funding for this work was provided by the US National Science Foundation, NSF OCE-1829981 (to TT), OCE-1756947 and OCE-1830033 (to DLV), and OCE-2023493 (to DB and ALP). Computational resources were provided by the Expanse system at the San Diego Supercomputer Center through allocation TG-OCE170017 from the Extreme Science and Engineering Discovery Environment (XSEDE), which was supported by National Science Foundation grant 1548562.

Code availability

The physical and biogeochemical codes used for our simulations can be accessed at: https://github.com/UCLA-ROMS/Code.

The model output can be accessed through Zenodo: (link will be provided before publication)

Data availability

In-situ benthic Fe flux data are accessible through the Biological & Chemical Oceanography Data Management Office (BCO-DMO) under the following DOI: 10.26008/1912/bco-dmo.896706.1.

Author contributions.

DR, TT, DB, and AP conceived this study. DM, DJY, FJ, FW, ECA, KMG, DLV and TT conducted the sampling at sea. DJY transformed and interpreted ROV Jason data. FJ and FW constructed and managed benthic flux chambers. DYJ and DR analyzed Fe(II) and assisted with the flux calculation. MM provided the compiled Fe measurements along the U.S. West Coast. AP and MS performed the model simulations. DR, DB, AP and TT wrote the manuscript with input from all co-authors.

Competing interests

566 Some authors are members of the editorial board of Biogeosciences. The peer-review process was

567 guided by an independent editor, and the authors have no other competing interests to declare.

568 **References**

569 Aumont, O., Ethé, C., Tagliabue, A., Bopp, L., and Gehlen, M.: PISCES-v2: An ocean
570 biogeochemical model for carbon and ecosystem studies, Geosci. Model Dev., 8, 2465–2513,
571 https://doi.org/10.5194/gmd-8-2465-2015, 2015.

572 Behl, R. J. and Kennett, J. P.: Brief interstadial events in the Santa Barbara basin, NE Pacific,
573 during the past 60 kyr, Nature, 379, 243–246, https://doi.org/10.1038/379243a0, 1996.

574 Biller, D. V. and Bruland, K. W.: Sources and distributions of Mn, Fe, Co, Ni, Cu, Zn, and Cd
575 relative to macronutrients along the central California coast during the spring and summer
576 upwelling season, Mar. Chem., 155, 50–70, https://doi.org/10.1016/j.marchem.2013.06.003,
577 2013.

578 Boiteau, R. M., Till, C. P., Coale, T. H., Fitzsimmons, J. N., Bruland, K. W., and Repeta, D. J.:
579 Patterns of iron and siderophore distributions across the California Current System, Limnol.
580 Oceanogr., 64, 376–389, https://doi.org/10.1002/lno.11046, 2019.

581 Bopp, L., Resplandy, L., Orr, J. C., Doney, S. C., Dunne, J. P., Gehlen, M., Halloran, P., Heinze,
582 C., Ilyina, T., Séférian, R., Tjiputra, J., and Vichi, M.: Multiple stressors of ocean ecosystems in
583 the 21st century: projections with CMIP5 models, Biogeosciences, 10, 6225–6245,
584 https://doi.org/10.5194/bg-10-6225-2013, 2013.

585 Brander, K., Cochrane, K., Barange, M., and Soto, D.: Climate Change Implications for Fisheries
586 and Aquaculture, in: Climate Change Impacts on Fisheries and Aquaculture, edited by: Phillips,
587 B. F. and Pérez-Ramírez, M., John Wiley & Sons, Ltd, Chichester, UK, 45–62,
588 https://doi.org/10.1002/9781119154051.ch3, 2017.

589 Bray, N. A., Keyes, A., and Morawitz, W. M. L.: The California Current system in the Southern
590 California Bight and the Santa Barbara Channel, J. Geophys. Res. Oceans, 104, 7695–7714,
591 https://doi.org/10.1029/1998JC900038, 1999.

592 Bruland, K. W., Rue, E. L., and Smith, G. J.: Iron and macronutrients in California coastal
593 upwelling regimes: Implications for diatom blooms, Limnol. Oceanogr., 46, 1661–1674,
594 https://doi.org/10.4319/lo.2001.46.7.1661, 2001.

595 Bruland, K. W., Middag, R., and Lohan, M. C.: Controls of Trace Metals in Seawater, in:
596 Treatise on Geochemistry, Elsevier, 19–51, https://doi.org/10.1016/B978-0-08-095975-7.00602-
597 1, 2014.

598 Bundy, R. M., Biller, D. V., Buck, K. N., Bruland, K. W., and Barbeau, K. A.: Distinct pools of
599 dissolved iron-binding ligands in the surface and benthic boundary layer of the California
600 Current, Limnol. Oceanogr., 59, 769–787, https://doi.org/10.4319/lo.2014.59.3.0769, 2014.

601 Bundy, R. M., Abdulla, H. A. N., Hatcher, P. G., Biller, D. V., Buck, K. N., and Barbeau, K. A.:
602 Iron-binding ligands and humic substances in the San Francisco Bay estuary and estuarine-

603 influenced shelf regions of coastal California, Mar. Chem., 173, 183–194,
604 https://doi.org/10.1016/j.marchem.2014.11.005, 2015.

605 Bundy, R. M., Jiang, M., Carter, M., and Barbeau, K. A.: Iron-Binding Ligands in the Southern
606 California Current System: Mechanistic Studies, Front. Mar. Sci., 3,
607 https://doi.org/10.3389/fmars.2016.00027, 2016.

608 Capet, X., Campos, E. J., and Paiva, A. M.: Submesoscale activity over the Argentinian shelf,
609 Geophys. Res. Lett., 35, https://doi.org/10.1029/2008GL034736, 2008.

610 Carr, M.-E. and Kearns, E. J.: Production regimes in four Eastern Boundary Current systems,
611 Deep Sea Res. Part II Top. Stud. Oceanogr., 50, 3199–3221,
612 https://doi.org/10.1016/j.dsr2.2003.07.015, 2003.

613 Chappell, P., Armbrust, E., Barbeau, K., Bundy, R., Moffett, J., Vedamati, J., and Jenkins, B.:
614 Patterns of diatom diversity correlate with dissolved trace metal concentrations and longitudinal
615 position in the northeast Pacific coastal-offshore transition zone, Mar. Ecol. Prog. Ser., 609, 69–
616 86, https://doi.org/10.3354/meps12810, 2019.

617 Chase, Z.: Iron, nutrient, and phytoplankton distributions in Oregon coastal waters, J. Geophys.
618 Res., 107, 3174, https://doi.org/10.1029/2001JC000987, 2002.

619 Chase, Z., Johnson, K. S., Elrod, V. A., Plant, J. N., Fitzwater, S. E., Pickell, L., and Sakamoto,
620 C. M.: Manganese and iron distributions off central California influenced by upwelling and shelf
621 width, Mar. Chem., 95, 235–254, https://doi.org/10.1016/j.marchem.2004.09.006, 2005.

622 Chavez, F. P. and Messié, M.: A comparison of Eastern Boundary Upwelling Ecosystems, Prog.
623 Oceanogr., 83, 80–96, https://doi.org/10.1016/j.pocean.2009.07.032, 2009.

624 Dale, A. W., Nickelsen, L., Scholz, F., Hensen, C., Oschlies, A., and Wallmann, K.: A revised
625 global estimate of dissolved iron fluxes from marine sediments: GLOBAL BENTHIC IRON
626 FLUXES, Glob. Biogeochem. Cycles, 29, 691–707, https://doi.org/10.1002/2014GB005017,
627 2015.

628 Damien, P., Bianchi, D., McWilliams, J. C., Kessouri, F., Deutsch, C., Chen, R., and Renault, L.:
629 Enhanced Biogeochemical Cycling Along the U.S. West Coast Shelf, Glob. Biogeochem.
630 Cycles, 37, e2022GB007572, https://doi.org/10.1029/2022GB007572, 2023.

631 Deutsch, C., Sarmiento, J. L., Sigman, D. M., Gruber, N., and Dunne, J. P.: Spatial coupling of
632 nitrogen inputs and losses in the ocean, Nature, 445, 163–167,
633 https://doi.org/10.1038/nature05392, 2007.

634 Deutsch, C., Brix, H., Ito, T., Frenzel, H., and Thompson, L.: Climate-Forced Variability of
635 Ocean Hypoxia, Science, 333, 336–339, https://doi.org/10.1126/science.1202422, 2011.

636 Deutsch, C., Frenzel, H., McWilliams, J. C., Renault, L., Kessouri, F., Howard, E., Liang, J.-H.,
637 Bianchi, D., and Yang, S.: Biogeochemical variability in the California Current System, Prog.
638 Oceanogr., 196, 102565, https://doi.org/10.1016/j.pocean.2021.102565, 2021.

639   Dijkstra, N., Kraal, P., Kuypers, M. M. M., Schnetger, B., and Slomp, C. P.: Are Iron-Phosphate
640   Minerals a Sink for Phosphorus in Anoxic Black Sea Sediments?, PLOS ONE, 9, e101139,
641   https://doi.org/10.1371/journal.pone.0101139, 2014.

642   Evans, N., Schroeder, I. D., Pozo Buil, M., Jacox, M. G., and Bograd, S. J.: Drivers of
643   Subsurface Deoxygenation in the Southern California Current System, Geophys. Res. Lett., 47,
644   https://doi.org/10.1029/2020GL089274, 2020.

645   Firme, G. F., Rue, E. L., Weeks, D. A., Bruland, K. W., and Hutchins, D. A.: Spatial and
646   temporal variability in phytoplankton iron limitation along the California coast and consequences
647   for Si, N, and C biogeochemistry: SPATIAL AND TEMPORAL VARIABILITY IN
648   PHYTOPLANKTON IRON, Glob. Biogeochem. Cycles, 17,
649   https://doi.org/10.1029/2001GB001824, 2003.

650   Furrer, G. and Wehrli, B.: Biogeochemical processes at the sediment-water interface:
651   measurements and modeling, Appl. Geochem., 8, 117–119, https://doi.org/10.1016/S0883-
652   2927(09)80021-8, 1993.

653   García-Reyes, M. and Largier, J.: Observations of increased wind-driven coastal upwelling off
654   central California, J. Geophys. Res., 115, C04011, https://doi.org/10.1029/2009JC005576, 2010.

655   Goericke, R., Bograd, S. J., and Grundle, D. S.: Denitrification and flushing of the Santa Barbara
656   Basin bottom waters, Deep Sea Res. Part II Top. Stud. Oceanogr., 112, 53–60,
657   https://doi.org/10.1016/j.dsr2.2014.07.012, 2015.

658   Grasshoff, K. and Ehrhardt, M.: Methods of seawater analysis, 3rd, completely rev. and extended
659   ed. ed., Wiley-VCH, Weinheim, New York, xxxii, 600 pp., 1999.

660   Hawco, N. J., Barone, B., Church, M. J., Babcock-Adams, L., Repeta, D. J., Wear, E. K.,
661   Foreman, R. K., Björkman, K. M., Bent, S., Van Mooy, B. A. S., Sheyn, U., DeLong, E. F.,
662   Acker, M., Kelly, R. L., Nelson, A., Ranieri, J., Clemente, T. M., Karl, D. M., and John, S. G.:
663   Iron Depletion in the Deep Chlorophyll Maximum: Mesoscale Eddies as Natural Iron
664   Fertilization Experiments, Glob. Biogeochem. Cycles, 35,
665   https://doi.org/10.1029/2021GB007112, 2021.

666   Hendershott and Winant: Surface Circulation in the Santa Barbara Channel, Oceanography, 9,
667   114–121, https://doi.org/10.5670/oceanog.1996.14, 1996.

668   Hogle, S. L., Dupont, C. L., Hopkinson, B. M., King, A. L., Buck, K. N., Roe, K. L., Stuart, R.
669   K., Allen, A. E., Mann, E. L., Johnson, Z. I., and Barbeau, K. A.: Pervasive iron limitation at
670   subsurface chlorophyll maxima of the California Current, Proc. Natl. Acad. Sci., 115, 13300–
671   13305, https://doi.org/10.1073/pnas.1813192115, 2018.

672   Homoky, W. B., Conway, T. M., John, S. G., König, D., Deng, F., Tagliabue, A., and Mills, R.
673   A.: Iron colloids dominate sedimentary supply to the ocean interior, Proc. Natl. Acad. Sci., 118,
674   e2016078118, https://doi.org/10.1073/pnas.2016078118, 2021.

675 John, S. G., Mendez, J., Moffett, J., and Adkins, J.: The flux of iron and iron isotopes from San
676 Pedro Basin sediments, Geochim. Cosmochim. Acta, 93, 14–29,
677 https://doi.org/10.1016/j.gca.2012.06.003, 2012.

678 Johnson, K. S., Elrod, V. A., Fitzwater, S. E., Plant, J. N., Chavez, F. P., Tanner, S. J., Gordon,
679 R. M., Westphal, D. L., Perry, K. D., Wu, J., and Karl, D. M.: Surface ocean-lower atmosphere
680 interactions in the Northeast Pacific Ocean Gyre: Aerosols, iron, and the ecosystem response,
681 Glob. Biogeochem. Cycles, 17, https://doi.org/10.1029/2002GB002004, 2003.

682 Jørgensen, B. B. and Nelson, D. C.: Sulfide oxidation in marine sediments: Geochemistry meets
683 microbiology, in: Sulfur Biogeochemistry - Past and Present, Geological Society of America,
684 https://doi.org/10.1130/0-8137-2379-5.63, 2004.

685 Kessouri, F., Bianchi, D., Renault, L., McWilliams, J. C., Frenzel, H., and Deutsch, C. A.:
686 Submesoscale Currents Modulate the Seasonal Cycle of Nutrients and Productivity in the
687 California Current System, Glob. Biogeochem. Cycles, 34, e2020GB006578,
688 https://doi.org/10.1029/2020GB006578, 2020.

689 King, A. L. and Barbeau, K. A.: Dissolved iron and macronutrient distributions in the southern
690 California Current System, J. Geophys. Res., 116, C03018,
691 https://doi.org/10.1029/2010JC006324, 2011.

692 Kononets, M., Tengberg, A., Nilsson, M., Ekeroth, N., Hylén, A., Robertson, E. K., van de
693 Velde, S., Bonaglia, S., Rütting, T., Blomqvist, S., and Hall, P. O. J.: In situ incubations with the
694 Gothenburg benthic chamber landers: Applications and quality control, J. Mar. Syst., 214,
695 103475, https://doi.org/10.1016/j.jmarsys.2020.103475, 2021.

696 Kwiatkowski, L., Torres, O., Bopp, L., Aumont, O., Chamberlain, M., Christian, J. R., Dunne, J.
697 P., Gehlen, M., Ilyina, T., John, J. G., Lenton, A., Li, H., Lovenduski, N. S., Orr, J. C., Palmieri,
698 J., Santana-Falcón, Y., Schwinger, J., Séférian, R., Stock, C. A., Tagliabue, A., Takano, Y.,
699 Tjiputra, J., Toyama, K., Tsujino, H., Watanabe, M., Yamamoto, A., Yool, A., and Ziehn, T.:
700 Twenty-first century ocean warming, acidification, deoxygenation, and upper-ocean nutrient and
701 primary production decline from CMIP6 model projections, Biogeosciences, 17, 3439–3470,
702 https://doi.org/10.5194/bg-17-3439-2020, 2020.

703 Mahowald, N. M., Muhs, D. R., Levis, S., Rasch, P. J., Yoshioka, M., Zender, C. S., and Luo, C.:
704 Change in atmospheric mineral aerosols in response to climate: Last glacial period, preindustrial,
705 modern, and doubled carbon dioxide climates: DUST RESPONSE TO CLIMATE, J. Geophys.
706 Res. Atmospheres, 111, n/a-n/a, https://doi.org/10.1029/2005JD006653, 2006.

707 McMahon, P. B. and Chapelle, F. H.: Microbial production of organic acids in aquitard
708 sediments and its role in aquifer geochemistry, Nature, 349, 233–235,
709 https://doi.org/10.1038/349233a0, 1991.

710 Middelburg, J. J. and Levin, L. A.: Coastal hypoxia and sediment biogeochemistry,
711 Biogeosciences, 6, 1273–1293, https://doi.org/10.5194/bg-6-1273-2009, 2009a.

712 Middelburg, J. J. and Levin, L. A.: Coastal hypoxia and sediment biogeochemistry, 1273–1293,
713 2009b.

714 Mills, M. M., Ridame, C., Davey, M., La Roche, J., and Geider, R. J.: Iron and phosphorus co-
715 limit nitrogen fixation in the eastern tropical North Atlantic, Nature, 429, 292–294,
716 https://doi.org/10.1038/nature02550, 2004.

717 Moore, J. K. and Braucher, O.: Sedimentary and mineral dust sources of dissolved iron to the
718 world ocean, Biogeosciences, 5, 631–656, https://doi.org/10.5194/bg-5-631, 2008.

719 Moore, J. K., Doney, S. C., Kleypas, J. A., Glover, D. M., and Fung, I. Y.: An intermediate
720 complexity marine ecosystem model for the global domain, Deep Sea Res. Part II Top. Stud.
721 Oceanogr., 49, 403–462, https://doi.org/10.1016/S0967-0645(01)00108-4, 2001.

722 Moore, J. K., Doney, S. C., and Lindsay, K.: Upper ocean ecosystem dynamics and iron cycling
723 in a global three-dimensional model: GLOBAL ECOSYSTEM-BIOGEOCHEMICAL MODEL,
724 Glob. Biogeochem. Cycles, 18, n/a-n/a, https://doi.org/10.1029/2004GB002220, 2004.

725 Noffke, A., Hensen, C., Sommer, S., Scholz, F., Bohlen, L., Mosch, T., Graco, M., and
726 Wallmann, K.: Benthic iron and phosphorus fluxes across the Peruvian oxygen minimum zone,
727 Limnol. Oceanogr., 57, 851–867, https://doi.org/10.4319/lo.2012.57.3.0851, 2012.

728 Pham, A. L. D. and Ito, T.: Formation and Maintenance of the GEOTRACES Subsurface-
729 Dissolved Iron Maxima in an Ocean Biogeochemistry Model, Glob. Biogeochem. Cycles, 32,
730 932–953, https://doi.org/10.1029/2017GB005852, 2018.

731 Pham, A. L. D. and Ito, T.: Ligand Binding Strength Explains the Distribution of Iron in the
732 North Atlantic Ocean, Geophys. Res. Lett., 46, 7500–7508,
733 https://doi.org/10.1029/2019GL083319, 2019.

734 Pozo Buil, M. and Di Lorenzo, E.: Decadal dynamics and predictability of oxygen and
735 subsurface tracers in the California Current System, Geophys. Res. Lett., 44, 4204–4213,
736 https://doi.org/10.1002/2017GL072931, 2017.

737 Qin, Q., Kinnaman, F. S., Gosselin, K. M., Liu, N., Treude, T., and Valentine, D. L.: Seasonality
738 of water column methane oxidation and deoxygenation in a dynamic marine environment,
739 Geochim. Cosmochim. Acta, 336, 219–230, https://doi.org/10.1016/j.gca.2022.09.017, 2022.

740 Reimers, C. E., Lange, C. B., Tabak, M., and Bernhard, J. M.: Seasonal spillover and varve
741 formation in the Santa Barbara Basin, California, Limnol. Oceanogr., 35, 1577–1585,
742 https://doi.org/10.4319/lo.1990.35.7.1577, 1990.

743 Renault, L., Deutsch, C., McWilliams, J. C., Frenzel, H., Liang, J.-H., and Colas, F.: Partial
744 decoupling of primary productivity from upwelling in the California Current system, Nat.
745 Geosci., 9, 505–508, https://doi.org/10.1038/ngeo2722, 2016.

746 Renault, L., McWilliams, J. C., Kessouri, F., Jousse, A., Frenzel, H., Chen, R., and Deutsch, C.:
747 Evaluation of high-resolution atmospheric and oceanic simulations of the California Current
748 System, Prog. Oceanogr., 195, 102564, https://doi.org/10.1016/j.pocean.2021.102564, 2021.

749 Sañudo-Wilhelmy, S., Kustka, A., Gobler, C., Hutchins, D., Yang, M., Lwiza, K., Burns, J.,
750 Raven, J., and Carpenter, E.: Phosphorus limitation of nitrogen fixation by Trichodesmium in the
751 central Atlantic Ocean, Nature, 411, 66–9, https://doi.org/10.1038/35075041, 2001.

752 Severmann, S., McManus, J., Berelson, W. M., and Hammond, D. E.: The continental shelf
753 benthic iron flux and its isotope composition, Geochim. Cosmochim. Acta, 74, 3984–4004,
754 https://doi.org/10.1016/j.gca.2010.04.022, 2010.

755 Shchepetkin, A. F.: An adaptive, Courant-number-dependent implicit scheme for vertical
756 advection in oceanic modeling, Ocean Model., 91, 38–69,
757 https://doi.org/10.1016/j.ocemod.2015.03.006, 2015.

758 Shchepetkin, A. F. and McWilliams, J. C.: The regional oceanic modeling system (ROMS): a
759 split-explicit, free-surface, topography-following-coordinate oceanic model, Ocean Model., 9,
760 347–404, https://doi.org/10.1016/j.ocemod.2004.08.002, 2005.

761 Shiller, A. M., Gieskes, J. M., and Brian Price, N.: Particulate iron and manganese in the Santa
762 Barbara Basin, California, Geochim. Cosmochim. Acta, 49, 1239–1249,
763 https://doi.org/10.1016/0016-7037(85)90013-4, 1985.

764 Sholkovitz, E. and Soutar, A.: Changes in the composition of the bottom water of the Santa
765 Barbara Basin: effect of turbidity currents, Deep Sea Res. Oceanogr. Abstr., 22, 13–21,
766 https://doi.org/10.1016/0011-7471(75)90014-5, 1975.

767 Sholkovitz, E. R. and Gieskes, J. M.: A PHYSICAL-CHEMICAL STUDY OF THE FLUSHING
768 OF THE SANTA BARBARA BASIN1: FLUSHING OF THE SANTA BARBARA BASIN,
769 Limnol. Oceanogr., 16, 479–489, https://doi.org/10.4319/lo.1971.16.3.0479, 1971.

770 Sigman, D. M., Robinson, R., Knapp, A. N., van Geen, A., McCorkle, D. C., Brandes, J. A., and
771 Thunell, R. C.: Distinguishing between water column and sedimentary denitrification in the
772 Santa Barbara Basin using the stable isotopes of nitrate, Geochem. Geophys. Geosystems, 4,
773 https://doi.org/10.1029/2002GC000384, 2003.

774 Soetaert, K., Middelburg, J. J., Herman, P. M. J., and Buis, K.: On the coupling of benthic and
775 pelagic biogeochemical models, Earth-Sci. Rev., 51, 173–201, https://doi.org/10.1016/S0012-
776 8252(00)00004-0, 2000.

777 Sommer, S., Gier, J., Treude, T., Lomnitz, U., Dengler, M., Cardich, J., and Dale, A. W.:
778 Depletion of oxygen, nitrate and nitrite in the Peruvian oxygen minimum zone cause an
779 imbalance of benthic nitrogen fluxes, Deep Sea Res. Part Oceanogr. Res. Pap., 112, 113–122,
780 https://doi.org/10.1016/j.dsr.2016.03.001, 2016.

781 Tagliabue, A., Sallée, J.-B., Bowie, A. R., Lévy, M., Swart, S., and Boyd, P. W.: Surface-water
782 iron supplies in the Southern Ocean sustained by deep winter mixing, Nat. Geosci., 7, 314–320,
783 https://doi.org/10.1038/ngeo2101, 2014.

784 Tagliabue, A., Aumont, O., DeAth, R., Dunne, J. P., Dutkiewicz, S., Galbraith, E., Misumi, K.,
785 Moore, J. K., Ridgwell, A., Sherman, E., Stock, C., Vichi, M., Völker, C., and Yool, A.: How
786 well do global ocean biogeochemistry models simulate dissolved iron distributions?: GLOBAL
787 IRON MODELS, Glob. Biogeochem. Cycles, 30, 149–174,
788 https://doi.org/10.1002/2015GB005289, 2016.

789 Tagliabue, A., Bowie, A. R., Boyd, P. W., Buck, K. N., Johnson, K. S., and Saito, M. A.: The
790 integral role of iron in ocean biogeochemistry, Nature, 543, 51–59,
791 https://doi.org/10.1038/nature21058, 2017.

792 Testa, J. M., Brady, D. C., Di Toro, D. M., Boynton, W. R., Cornwell, J. C., and Kemp, W. M.:
793 Sediment flux modeling: Simulating nitrogen, phosphorus, and silica cycles, Estuar. Coast. Shelf
794 Sci., 131, 245–263, https://doi.org/10.1016/j.ecss.2013.06.014, 2013.

795 Till, C. P., Solomon, J. R., Cohen, N. R., Lampe, R. H., Marchetti, A., Coale, T. H., and Bruland,
796 K. W.: The iron limitation mosaic in the California Current System: Factors governing Fe
797 availability in the shelf/near-shelf region, Limnol. Oceanogr., 64, 109–123,
798 https://doi.org/10.1002/lno.11022, 2019.

799 Treude, T., Smith, C. R., Wenzhöfer, F., Carney, E., Bernardino, A. F., Hannides, A. K., Krüger,
800 M., and Boetius, A.: Biogeochemistry of a deep-sea whale fall: sulfate reduction, sulfide efflux
801 and methanogenesis, Mar. Ecol. Prog. Ser., 382, 1–21, 2009.

802 Valentine, D. L., Fisher, G. B., Pizarro, O., Kaiser, C. L., Yoerger, D., Breier, J. A., and Tarn, J.:
803 Autonomous Marine Robotic Technology Reveals an Expansive Benthic Bacterial Community
804 Relevant to Regional Nitrogen Biogeochemistry, Environ. Sci. Technol., 50, 11057–11065,
805 https://doi.org/10.1021/acs.est.6b03584, 2016.

806 Wallmann, K., José, Y. S., Hopwood, M. J., Somes, C. J., Dale, A. W., Scholz, F., Achterberg,
807 E. P., and Oschlies, A.: Biogeochemical feedbacks may amplify ongoing and future ocean
808 deoxygenation: a case study from the Peruvian oxygen minimum zone, Biogeochemistry, 159,
809 45–67, https://doi.org/10.1007/s10533-022-00908-w, 2022.

810 White, M. E., Rafter, P. A., Stephens, B. M., Wankel, S. D., and Aluwihare, L. I.: Recent
811 Increases in Water Column Denitrification in the Seasonally Suboxic Bottom Waters of the
812 Santa Barbara Basin, Geophys. Res. Lett., 46, 6786–6795,
813 https://doi.org/10.1029/2019GL082075, 2019.

814 Widdows, J. and Brinsley, M.: Impact of biotic and abiotic processes on sediment dynamics and
815 the consequences to the structure and functioning of the intertidal zone, J. Sea Res., 48, 143–156,
816 https://doi.org/10.1016/S1385-1101(02)00148-X, 2002.

817   Yao, M., Henny, C., and Maresca, J. A.: Freshwater Bacteria Release Methane as a By-Product
818   of Phosphorus Acquisition, Appl. Environ. Microbiol., 82, 6994–7003,
819   https://doi.org/10.1128/AEM.02399-16, 2016.

820   Yousavich, D. J., Robinson, D., Peng, X., Krause, S. J. E., Wenzhoefer, F., Janßen, F., Liu, N.,
821   Tarn, J., Kinnaman, F., Valentine, D. L., and Treude, T.: Marine anoxia initiates giant sulfur-
822   bacteria mat proliferation and associated changes in benthic nitrogen, sulfur, and iron cycling in
823   the Santa Barbara Basin, California Borderland, EGUsphere, 1–48,
824   https://doi.org/10.5194/egusphere-2023-1198, 2023.

825   Zhou, Y., Gong, H., and Zhou, F.: Responses of Horizontally Expanding Oceanic Oxygen
826   Minimum Zones to Climate Change Based on Observations, Geophys. Res. Lett., 49,
827   e2022GL097724, https://doi.org/10.1029/2022GL097724, 2022.

828